Solution Structure of an Alternate Conformation of Helix 27 from *Escherichia coli* 16S rRNA

Meredith Newby Spano,* Nils G. Walter
Department of Chemistry, University of Michigan, 930 N. University Ave., Ann Arbor, MI 48109-1055

Received 20 August 2010; revised 8 March 2011; accepted 9 March 2011
Published online 25 March 2011 in Wiley Online Library (wileyonlinelibrary.com). DOI 10.1002/bip.21626

ABSTRACT:

Helix (H)27 of 16S ribosomal (r)RNA from Escherichia coli *was dubbed the "switch helix" when mutagenesis suggested that two alternative base pair registers may have distinct functional roles in the bacterial ribosome. Although more recent genetic analyses suggest that H27 conformational switching is not required for translation, previous solution studies demonstrated that the isolated* E. coli *H27 can dynamically convert between the 885 and 888 conformations. Here, we have solved the nuclear magnetic resonance solution structure of a locked 888 conformation. NOE and residual dipolar coupling restraints reveal an architecture that markedly differs from that of the 885 conformation found in crystal structures of the bacterial ribosome. In place of the loop E motif that characterizes the 885 conformer and that the 888 conformer cannot adopt, we find evidence for an asymmetrical A-rich internal loop stabilized by stacking interactions among the unpaired A's. Comparison of the isolated H27 888 solution structure with the 885 crystal structure within the context of the ribosome suggests a difference in overall length of H27 that presents one plausible reason for the absence of H27 conformational switching within the sterically confining ribosome. © 2011 Wiley Periodicals, Inc. Biopolymers 95: 653–668, 2011.*

Keywords: solution NMR spectroscopy; RNA structure; internal loop; ribosome; RNA–metal ion interactions

This article was originally published online as an accepted preprint. The "Published Online" date corresponds to the preprint version. You can request a copy of the preprint by emailing the Biopolymers editorial office at biopolymers@wiley.com

INTRODUCTION

Helix (H)27 is centrally located within the decoding center of the small ribosomal subunit, comprising nucleotides (nt) 885-912 in *E. coli* 16S ribosomal (r)RNA (Figure 1A). It is one of the most conserved sequences within the ribosome; 23 of its 28 nucleotides are at least 90% conserved among bacteria.[1] Early sequence alignment of 16S rRNA predicted a base pair between C912 and G888.[2] Based on systematic mutagenesis and genetic analysis of *E. coli* 16S ribosomal (r)RNA, a model was developed predicting that this secondary structure, termed the "888 conformation," reversibly changes into an alternate "885 conformation," with a base pair between C912 and G885 instead (Figure 1B), as a prerequisite for the correct decoding of the messenger (m)RNA during translation.[3] Such conformational switching of H27 can be envisioned through a simple slippage of the 3′ CUC triplet from base pairing with the 5′ GGG triplet (in the 885 conformation) to pairing with the immediately downstream GAG triplet (in the 888 conformation). Fluorescence resonance energy transfer (FRET) and nuclear magnetic resonance (NMR) data of the isolated H27 further supported the existence of a

Additional Supporting Information may be found in the online version of this article.

Correspondence to: Nils G. Walter; e-mail: nwalter@umich.edu or Meredith Newby Spano; e-mail: mnewby@clemson.edu
**Present address:* Department of Physics and Astronomy, Clemson University, 215 Kinard Laboratory, Clemson, SC 29634-0978.

Contract grant sponsor: NIH
Contract grant number: GM62357
Contract grant sponsor: Camille Dreyfus Teacher-Scholar Award
Contract grant sponsor: NIH Ruth L. Kirschstein NRSA postdoctoral fellowship

dynamic equilibrium between the two conformations, with an interconversion rate on the millisecond timescale.[4] However, crystal structures of wild-type (WT) and hyperaccurate *E. coli* ribosomes,[5] as well as of the small subunit in both open and closed conformations,[6] found only the 885 conformation. Subsequent studies revealed that synergistic effects between the mutations within H27 and those used as selectable markers were responsible for the "error-prone" and "hyperaccurate" phenotypes observed in the original mutagenesis studies in *E. coli*.[7] Yet, the question remains why slippage between the 885 and 888 conformations does not occur in H27 of the *E. coli* ribosome, when it is apparently of low energetic barrier in the isolated helix.

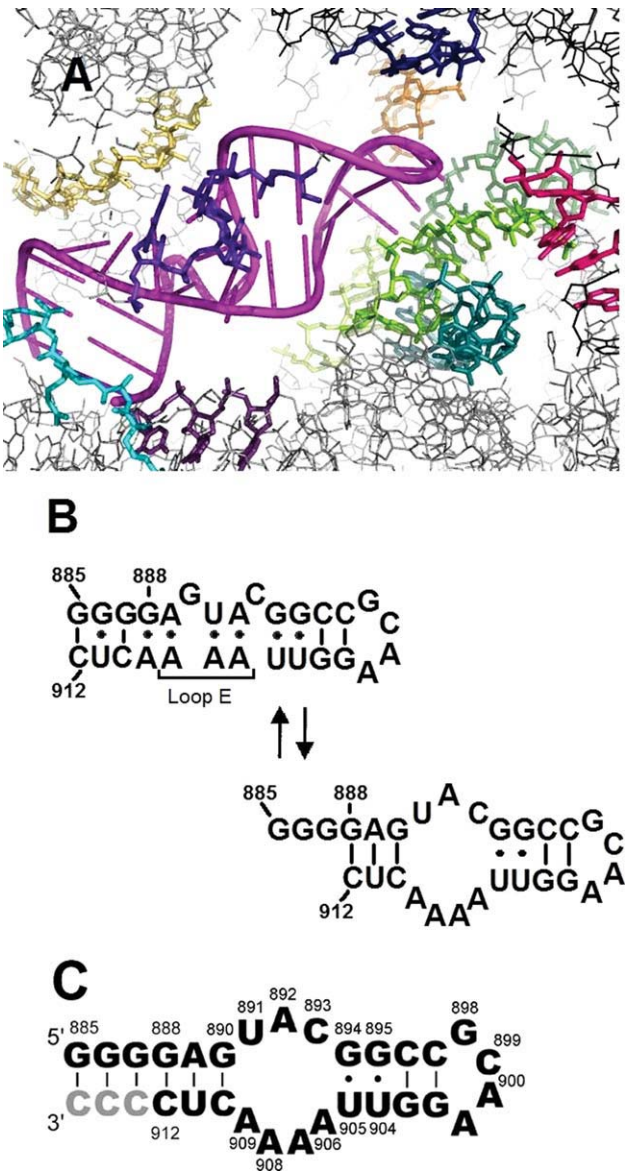

"Slippery" sequences are common in RNAs that exhibit conformational dynamics required for function, for example, the substrate helix of the *Neurospora* Varkud Satellite ribozyme,[8,9] and the HIV-1 frame shift inducing stem-loop.[10,11] Evolutionary analysis of rRNA structure predicts a trend over time toward an increased structural dependence upon proteins and both fewer and smaller scale motions within the rRNA itself.[12] It is unknown whether conformational switching within H27 may have served a biological purpose in ancient protoribosomes; however, such helical dynamics clearly appear to be suppressed within the context of the modern ribosome. How the ribosome prevents slippage within H27 is not known, as no protein side chain makes direct contact with specific nucleobases. However, basic residues within the N-terminus of the small ribosomal subunit protein S12 do make electrostatic contact with portions of the H27 backbone (Figure 1A). In addition, our previous NMR and FRET studies of metal ion binding sites within an isolated helix representing the 885 conformer suggested that magnesium ions may also stabilize the global conformation of H27.[13]

Here, we present the solution NMR structure of a conformationally "locked" helix representing the alternate 888 conformation of H27 (Figures 1B and 1C). We find evidence for an asymmetrical A-rich internal loop, characterized by stacking interactions among the unpaired adenines and some slight conformational variability. Comparison of the relatively elongated global architecture of the 888 conformation

FIGURE 1 H27 comprises nucleotides 885-912 of *Escherichia coli* 16S rRNA. (A) A slice through the ribosome reveals the bases and amino acids in close proximity to H27 (PDB identification numbers 2AVY and 2AW4). The large ribosomal subunit is colored black, and the small subunit is shown in gray. H27 is located in the center of Figure A in magenta as a cartoon, and all RNA and/or protein within ~ 10 Å of the helix is shown and colored. A portion of S12 (Arg 11–Ala 22) is colored in cyan, lower left; U243-245 of 16S rRNA is colored purple, center; C1412-G1415 of 16S rRNA is colored yellow, upper left; U1692-G1695 of 23S rRNA is shown in navy blue, upper right corner; G1831-C1832 of 23S rRNA is shown in orange, upper right; G809-U813 of 16S rRNA is shown in bright green, on the right; U762-A768 of 16S rRNA are shown in teal, on the right; G1511-A1513 of 16S rRNA is colored yellow-green, on the right; G769-G771 of 16S rRNA is colored dark green, on the right; A716-C719 of 23S rRNA is shown in hot pink, far right. (B) 912-885 (top) and 912-888 (bottom) conformations originally proposed by Lodmell and Dahlberg. (C) Molecular construct used for NMR studies representing the alternate 888 conformation of H27 from of *E. coli* 16S rRNA. Black nucleotides represent the wild-type sequence; grey nucleotides at the terminus of the lower stem were added to the 3′ end of the *E. coli* native sequence to favor the 888 conformation over the 885.

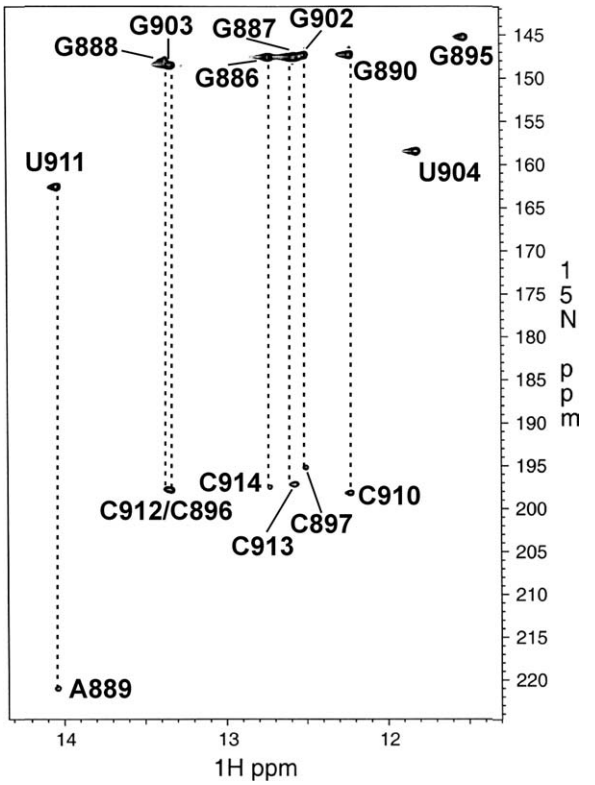

FIGURE 2 J_{NN}-COSY spectrum of 888_{locked}. Connectivities are drawn (dashed lines) between each imino proton-nitrogen resonance pair, indicative of Watson–Crick base pairing. Imino proton assignments are labeled next to each U and G imino proton-nitrogen resonances and the resonances belonging to their respective Watson–Crick base pairing partners.

with that of the 885 conformation, as observed in X-ray crystal structures, suggests steric clash as one possible explanation for the absence of conformational slippage within H27 of modern ribosomes.

RESULTS

Resonance Assignments and Investigation of Structural Features by NMR

Base pairing patterns were established through J_{NN}-correlation spectroscopy (COSY) (see Figure 2) of the uniformly $^{13}C/^{15}N$-labeled 888 NMR construct, henceforth termed 888_{locked}. This RNA is characterized by a "lower stem," consisting of six Watson–Crick base pairs that form the helix terminus and an "upper stem" comprising two G-U wobble pairs flanked by two canonical C-G pairs and capped with a GCAA tetraloop. An A-rich internal loop is situated between the upper and lower stems (Figure 1C). Initial imino proton assignments were made via standard homonuclear nuclear Overhauser effect spectroscopy (NOESY)-based methods at 278 K.[14] Through-bond coherence transfer revealed seven stable Watson–Crick base pairs in 888_{locked}, G886-C914, G887-C913, G888-C912, A889-U911, G890-C910, G903-C896, and G902-C897. In addition, imino proton resonances belonging to U904 and G895 displayed a strong cross peak in NOESY, characteristic of a G-U wobble pair,[15] and the G898 imino resonance was observed at 10.51 parts per million (ppm), an upfield position typical for G imino protons in GNRA tetraloops.[16] The G885 imino resonance was not visible in any spectrum, most likely because of end-fraying effects.[17]

Since no imino protons were observed from U891, G894, or U905, it was difficult to gather information about the internal loop structure directly from J_{NN}-COSY and NOESY of exchangeable protons. Instead, we performed specific experiments with the intent to either verify or rule out the existence of possible base–base interactions within the internal loop. To identify a possible A^+-C pair between A906 and C893, $^1H–^{13}C$ heteronuclear single-quantum coherence (HSQC) spectra, optimized for observation of base C6/C8 and A(C2) resonances, were collected at a pH as low as 4.61, given that an adenine protonated at the N1 position will display a characteristically upfield-shifted C2 resonance at slightly acidic pH.[18,19] No significant shifting of any adenine C2 resonance was observed (see Supporting Information for spectra). Ten millimolar magnesium chloride was added to the sample at pH 6.4 in an effort to stabilize any transient A^+-C pair, and again, no upfield-shifted adenine C2 resonance was observed in HSQC spectra. NMR experiments are therefore consistent with the absence of an A^+-C pair within the internal loop of 888_{locked} under a variety of pH and ionic strength conditions.

To investigate the possibility of sheared A-A pairs within the internal loop of 888_{locked}, an H(CN)N(H) experiment was performed. This pulse sequence was optimized for through-hydrogen-bond coherence transfer between purine H8 protons and hydrogen-bonded amino nitrogens via C8 and N7.[20] Using this strategy, a *trans* Watson–Crick/Hoogsteen or *trans* Hoogsteen/Hoogsteen interaction can be identified between two adenines, even if the amino protons involved in coherence transfer are extremely exchange-broadened. However, no resonances were observed for 888_{locked} that would indicate the presence of these types of sheared A-A pairs in the internal loop (data not shown). This absence of such AH8-N6 resonances in our H(CN)N(H) spectrum alone does not rule out the possibility of other types of base pairing interactions between adenines within the internal loop, such as *cis* Watson–Crick/Watson–Crick, *trans* Watson–Crick/Watson–Crick, *cis* Watson–Crick/sugar edge, *trans* Watson–Crick/sugar-edge, *cis* Hoogsteen/sugar-edge, *trans*

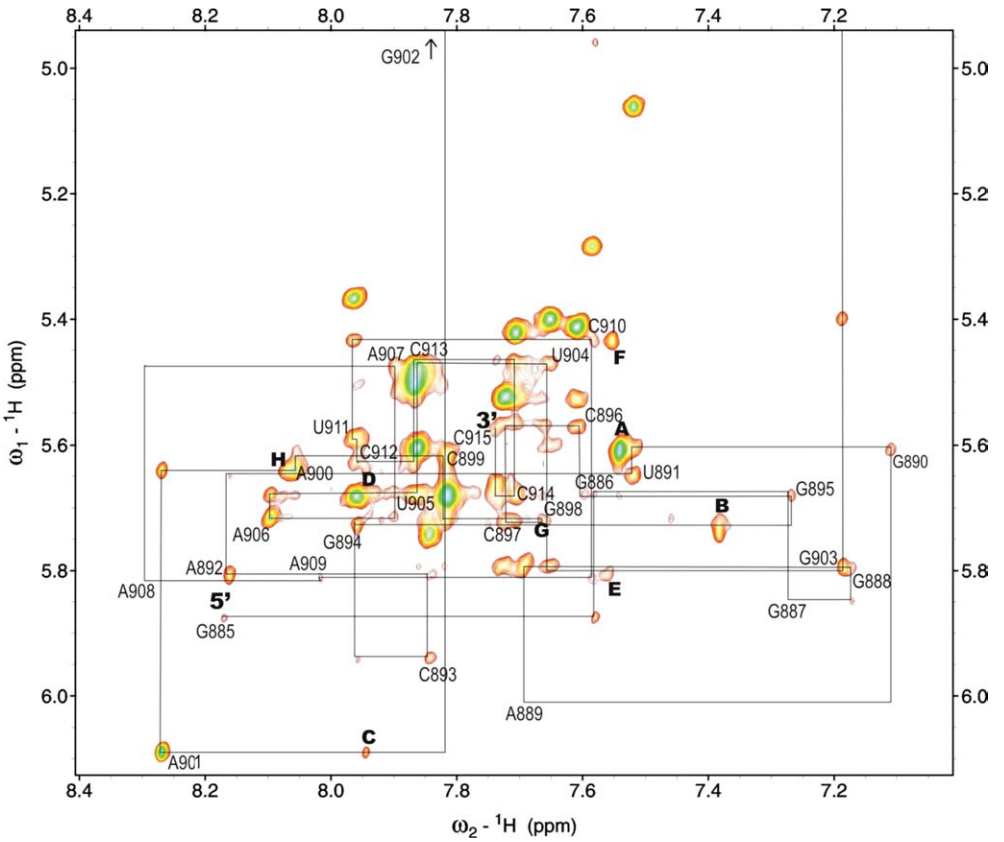

FIGURE 3 Aromatic-anomeric connectivities are nearly continuous throughout the molecule, as shown for the base-H1′region of a 450-ms mixing time NOESY acquired at 30°C. Nucleotides are labeled next to their respective intranucleotide base-H1′ cross peak. Some key AH2 NOEs are also labeled: (A) A889H2-G890H1′ and A889H2-C912H1′; (B) A906H2-G894H1′ and A906H2-C893H5; (C) A900H2-A901H1′; (D) A900H2- H1′; (E) A909H2-A892H1′ and A907H2-A908H1′; (F) A909H2-C910H1′; (G) A892H2-A906H1′; and (H) A901H2-A900H1′.

Hoogsteen/sugar-edge, *cis* sugar-edge/sugar-edge, and *trans* sugar-edge/sugar-edge. However, these results, when taken together with our NOE data, are consistent with only one possible interstrand A-A interaction, a *trans* Hoogsteen/sugar-edge pair between A892 and A908. We do not observe an A892 H2-A908 H8 NOE; however, that would support the presence of this sheared A-A pair, suggesting that such a pair, if it exists, is transient in nature.

NOESY of nonexchangeable protons were acquired at a number of mixing times to assess the buildup rate of nuclear Overhauser effects (NOEs) and aid in assignment of overlapped resonances. Pyrimidine H6 resonances were assigned via total correlation spectroscopy (TOCSY) H5-H6 cross peaks (see Supporting Information), and aromatic–anomeric connectivities were nearly continuous throughout the molecule, as shown in Figure 3. However, relatively long (450 ms) mixing times were required to obtain base-H1′ connectivities throughout the internal loop region of the molecule. Additionally, spectra acquired at 30°C were much better resolved than those acquired at 20°C, which displayed signs of exchange-broadening. Chemical shift data for resonances at 303 K are provided in Supporting Information. These data, taken together with the observation that exchangeable protons within the internal loop gave rise to extremely broad resonances because of rapid exchange, strongly suggested that bases within the internal loop of 888_{locked} are dynamic on the NMR timescale.

The absence of restraints from an A+-C pair or sheared A-A pairs, together with the absence of NOEs from internal loop amino protons, make the assignment of adenine H2 resonances extremely important, since distance restraints in the internal loop will rely on NOEs involving these protons. Several key NOEs involving adenine H2 proton resonances are labeled in Figure 3 and indicated on the NOE diagram shown in Figure 4. The A909(H2) resonance displays NOEs to the C910(H1′) and A892(H1′) resonances; these H2-H1′$_{i+1}$ and cross strand H2-H1′$_{i-1}$ NOEs are typical of A-form helix geometries, suggesting that this region of the

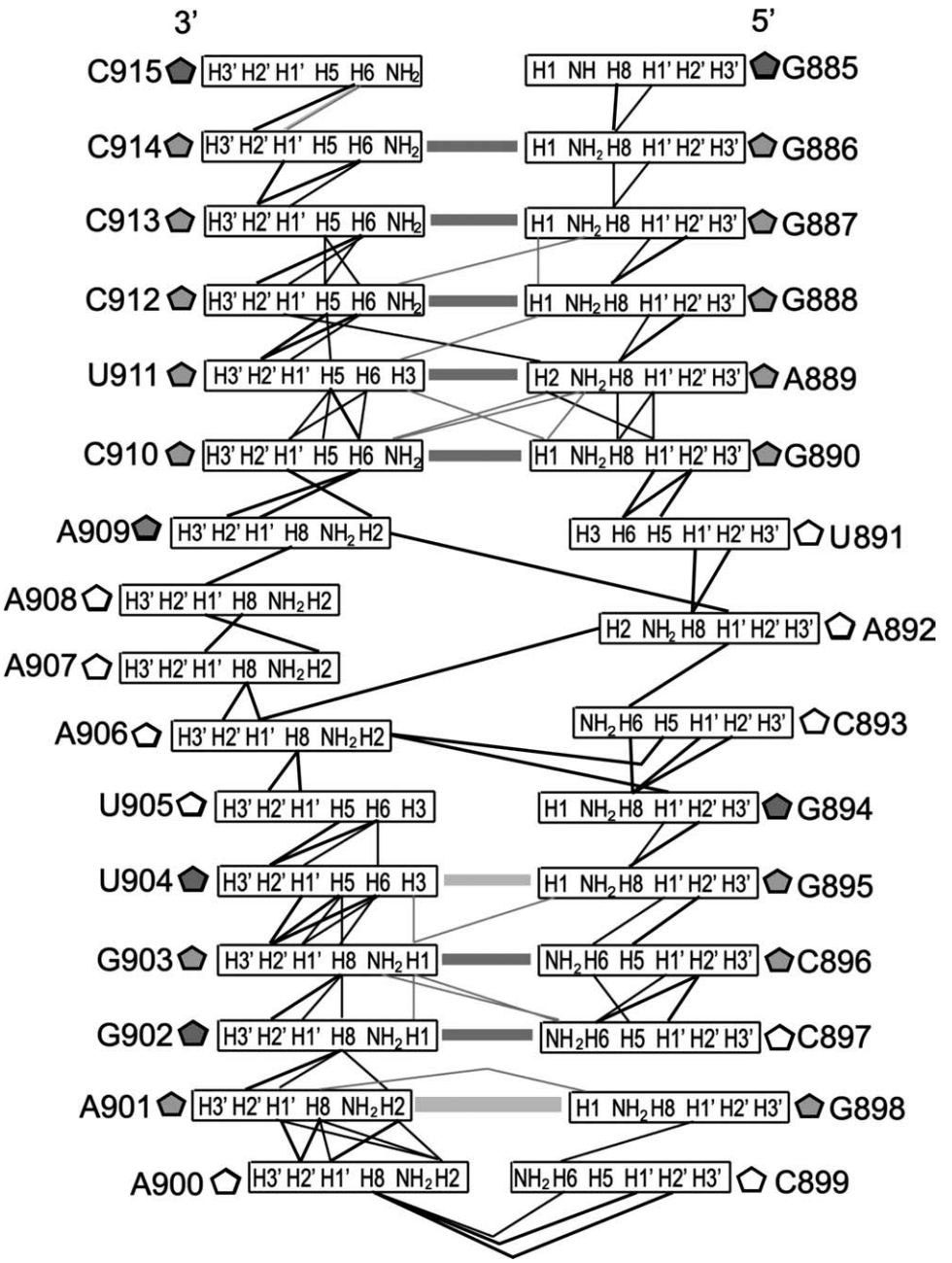

FIGURE 4 NOE diagram showing key internucleotide interactions involving H27 888 base protons. Thin black lines represent NOEs, and thick grey lines represent Watson–Crick base pairs observed via J_{NN}-COSY spectra. Thick light grey lines between bases represent non-Watson–Crick hydrogen bonding interactions supported by NOE and/or chemical shift data. White and grey-shaded pentagons next to nucleotide labels represent ribose puckers, with white signifying predominantly C2′-endo and grey indicating predominantly C3′-endo conformations.

internal loop assumes an architecture similar to that of the lower helical portion of the molecule. The A907(H2) resonance also displays an H2-H1′$_{i+1}$ NOE to A908 H1′; however, no cross strand NOEs are observed. The A906 H2 resonance does display a cross strand NOE to G894(H1′); however, it also exhibits an unusual NOE to C893 H5, whereas the A892(H2) resonance also displays an unusual NOE to A906(H1′), indicating some deviation from usual canonical parameters in the vicinity of these bases.

TOCSY spectra revealed strong cross peaks in specific regions representing relatively large $J_{H1'\text{-}H2'}$ couplings (>7 Hz) involving resonances belonging to every nucleotide

Table I Structural Statistics

Distance restraints	449
Intranucleotide NOEs	179
Internucleotide NOEs	200
Hydrogen bond restraints	70
Dihedral restraints	417
Residual dipolar couplings	20 (6)[a]
rms deviations from experimental restraints	
Distance restraints (Å)	0.162
Dihedral restraints (°)	0.057
rms deviations from idealized covalent geometry	
Bond lengths (Å)	0.006
Bond angles (°)	1.188
Impropers (deg.)	0.612
Mean pairwise rmsd for low-energy ensemble, all atoms	
Entire Molecule	5.38 ± 2.53 Å
Internal Loop (U891-G894 and U905-A909)	4.72 ± 1.50 Å
Upper stem (G895-U904)	0.95 ± 0.33 Å
Lower Stem (G885-G890 and C910-C915)	0.52 ± 0.19 Å

[a] The number in parentheses denotes the number of RDC's excluded from refinement, and used for cross-validation.

within the internal loop region of the molecule except for A909 (see Supporting Information for spectrum). These large scalar coupling constants indicate strong C2′-endo character for riboses within this region of 888_{locked}, and the broadness of the cross peaks, especially in the H2′ dimension, suggest conformational flexibility for these sugars. Riboses for which these strong TOCSY cross peaks were observed were defined as C2′-endo conformers in structure calculations.

Structure Calculations Using Residual Dipolar Couplings

Energies for random starting structures generated from the 888_{locked} primary sequence were minimized in X-PLOR,[21] as described in "Materials and Methods" using 449 NOE-derived restraints (an average of 14.5 per residue), 70 individually imposed hydrogen bonds, and backbone dihedral angles that were restrained to model A-type helical values for upper and lower stem nucleotides within canonically base-paired regions of the RNA (Table I). All glycosidic χ angles were restrained to reflect the *anti*-conformation because of the absence of strong intranucleotide H6/H8-H1′ NOEs at 50-ms mixing times indicative of syn base conformations. Additionally, ribose conformations of all nucleotides were restrained to C3′-endo parameters, except for those belonging to U891, A892, C893, C897, C899, A900, U905, A906, A907, and A908, which were restrained to the C2′-endo conformation, because they displayed strong H1′-H2′ cross peaks in TOCSY spectra, indicating $J_{H1'\text{-}H2'} > 7$ Hz. Twenty residual dipolar couplings (RDCs; ~ 70% of the available helical stem data) were then used, along with RNA database potentials, to refine the global conformations of the 50 lowest energy structures using XPLOR-NIH,[22] as described.[23,24] The six remaining RDCs were used for structure cross-validation and prediction of R_{free} values (see Supporting Information).[25] Axial and rhombic alignment tensors (D_a and R, respectively) for the upper and lower stems of 888_{locked} were determined from a powder-pattern analysis (see Supporting Information).[24] Structures were refined using two independent techniques, one using D_a and R defined separately for the upper stem and the lower stem of the molecule and one using a single set of globally defined alignment tensors. R_{free} values were lower for the set of structures that used two sets of alignment tensors, and these 13 structures with R_{free} values <30 comprised the final ensemble structure reported.

The resulting ensemble of NMR structures of 888_{locked} have an overall pairwise root-mean-square-deviation (rmsd) of 5.38 Å (Table I), with the rmsd values for the upper stem (G895-U904) and lower stem (G885-G890, C910-C915) considerably smaller (0.95 Å and 0.52 Å, respectively). These stem regions conform to the enforced A-type helix geometry (see Figure 5), whereas the capping GCAA tetraloop adopts a well-characterized conformation.[16] By contrast, the rmsd among internal loop nucleotides (U891-G894, U905-A909) is comparatively high, 4.72 Å (Table I). Because of a lower average number of NOE and dihedral angle restraints available for the internal loop region of the molecule as compared with the upper and lower stems, there is more conformational variability observed within the internal loop region than the Watson–Crick base-pairs and the tetraloop of 888_{locked}. For example, in four of the lowest energy structures, bases C893 and A908 reside in an extrahelical conformation. In two of the structures, A907 and A908 are bulged out of the helix, stacked in a coplanar conformation. $^{1}H\text{-}^{15}N$ NOE measurements recorded for the proton-nitrogen imino pairs within 888_{locked} demonstrate that NOEs within the internal loop region are on average ~ 15% weaker than those measured for the upper and lower stem regions (see Supporting Information), suggesting a comparatively higher amount of dynamics in the internal loop, as compared with the rest of the RNA.

Despite the differences observed in internal loop architecture among the low-energy structures, there are several similarities among them. In all of the structures, internal loop bases A909 and U891, which were not enforced to base pair by hydrogen bonding restraints in the structure calculations, form either a Watson–Crick base pair or form a hydrogen bond via A909(N6) and U891(O4). A common feature of the

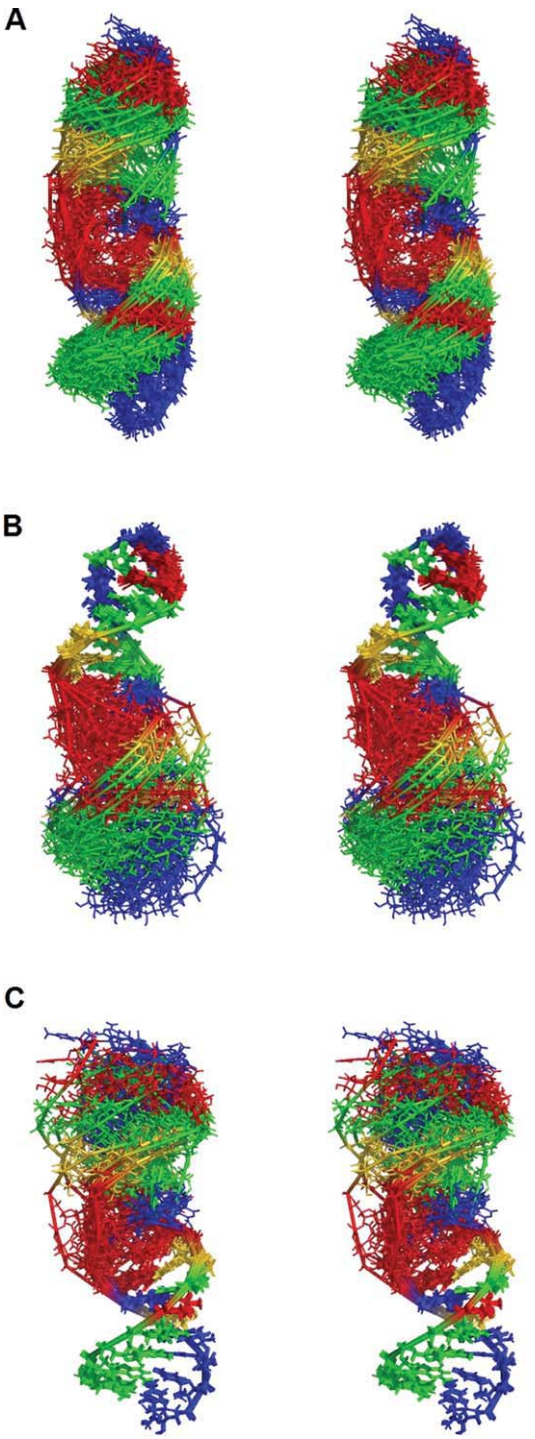

FIGURE 5 Stereo views of the ensemble H27 888 structure (guanines are colored green, uracils gold, cytosines blue, and adenines red). (A) The 13 low-energy structures selected had R_{free} values <30 after RDC and nucleic acid database refinement. Structures superimposed over all atoms. (B) Pair-wise superposition performed for the lower stem of the molecule (G885-G890, C910-C915). (C) Pair-wise superposition performed for the upper stem of the molecule (G895-U904). This figure was created using PyMol software.

internal loop is the conformation of A906, which stacks on U905 and deviates little from A-form geometry (Figures 6A and 6B). Another common feature of the internal loop is the relative absence of canonical Watson–Crick pairing and hydrogen bonding in the region, except for A909-U891. Instead, abundant stacking interactions are observed throughout the internal loop, especially among the adjacent adenine bases; two unpaired adenines, A906 and A907 in most structures, appear to be particularly stabilized by adjacent π-stacking. The stabilization of the internal loop conformation by π-stacking rather than canonical Watson–Crick hydrogen bonding results in a widening of the major groove throughout this portion of the molecule. The major groove width across the asymmetric internal loop (measured from phosphate to phosphate) is more than 19 Å for all structures, as compared with $\sim$ 11 Å for a model A-form helix.[26] Consequently, the H27 helix appears to be "under-wound" as compared with typical A-form helices (Figure 6C). A standard A-form double helix forms an open cylinder along the helix axis with a van der Waals radius of $\sim$ 3.5 Å.[27] No open cylinder is observed along the helical axis of the 888_{locked} structure because of the deviation from canonical A-form parameters within the internal loop region, notably the under-winding of the helix and displacement of internal loop bases into the widened major groove. In all of the structures, at least one of the internal loop bases, A892, C893, A906, A907, and/or A908 are displaced toward the major groove. In two of the structures, displacement of A892 toward the major groove results in an unusual *trans* Hoogsteen/sugar-edge pairing forms between this adenine and A908 on the opposing strand (Figure 6E); that is, the amino group of A908 is within hydrogen bonding distance of A892(N3) ring nitrogen. We do, in fact, observe this interaction in two of our 13 low-energy structures. The absence of a strong NOE between A892 H2 and A908 H8, and thus the low number of structures containing this sheared A-A pair, suggests that the interaction is likely to be transient within the dynamic internal loop. It is also possible that it is an artifact of the calculation, since no NOEs exist to rule out the possibility of this unusual A-A interaction.

All structures of the NMR ensemble are very linear, having little to no bend along their helical axis. Global structural similarities may be attributed to the fact that the reported structures were refined using a single set of globally defined alignment tensors. However, structures determined using axial and rhombic alignment tensors D_a and R defined separately for the upper stem and the lower stem of the RNA were nearly identical (although R_{free} values were slightly higher for this set of structures, data not shown).

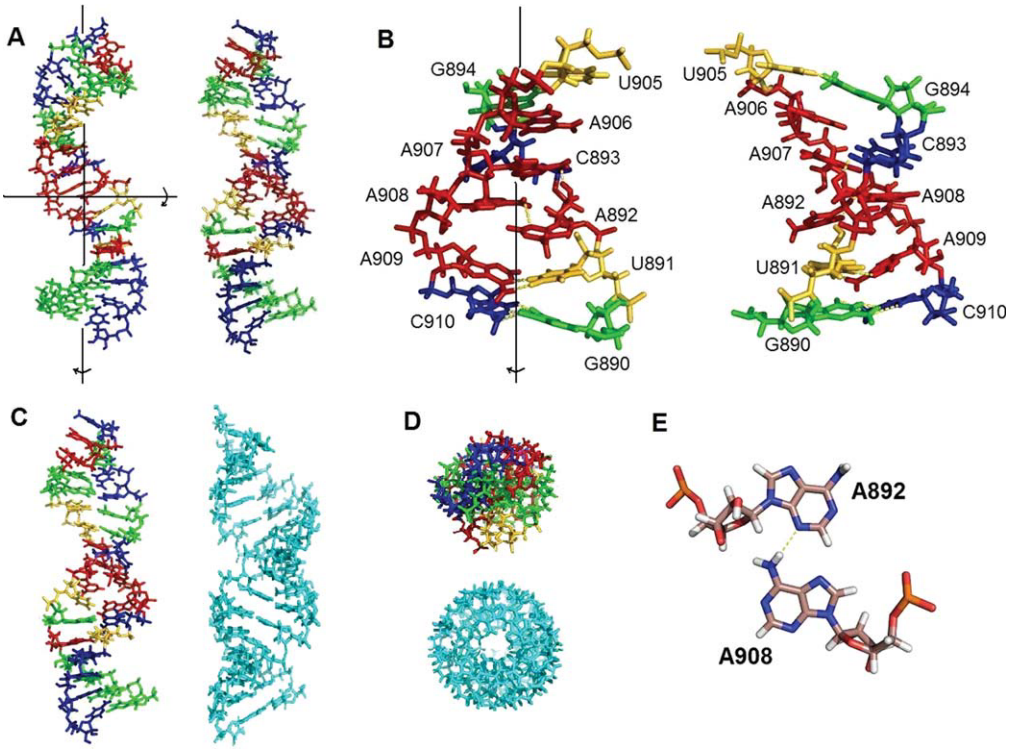

FIGURE 6 Details of the 888_{locked} structure. (A) Views of a representative 888_{locked} structure. Guanines are colored green, uracils gold, cytosines blue, and adenines red. The structure on the right shows the same structure ~ 180° rotated along the vertical axis from the depiction on the left. (B) Internal loop nucleotides G890-G894 and U905-C910, showing "major groove" interactions. Dashed yellow lines are drawn between donor and acceptor groups within hydrogen bonding distance of each other: A892(N6)-A908(N3); A892(2′OH)-C893(phosphate oxygen); G890-C10 and U891-A909 have dashed lines drawn between their respective Watson–Crick hydrogen-binding functionalities; and G894-U905 form a G-U wobble and have dashed lines drawn between U905(O2)-G895(N1) and U905(N3)-G895(O6). (C) Representative 888_{locked} structure, as shown in A, and a 16-base pair A-form helix showing A-form helical structure, in cyan (PDB 2KYD). (D) Also shown is the same representative 888_{locked} structure as viewed from the top of the helix or rotated 90° about the horizontal line shown in panel A. Below it is the same A-form structure shown in Panel C from the same view, in cyan. (E) The unusual *trans* sugar-edge/Hoogsteen-edge pairing between A892 and A908 in a portion of the structures is shown. This figure was created using PyMol software.

Multivalent Metal Ion Interactions Within 888_{locked}

Crystal structures of the bacterial 30S ribosomal subunit have identified two specific Mg^{2+} binding sites within the 885 conformation of H27,[6,28–30] one adjacent to the major groove edge of a G-U pair in the lower stem portion of the helix and another within the GNRA tetraloop, a commonly recognized metal ion binding site.[31–34] Previous NMR spectroscopic studies have described additional RNA–metal interactions of the 885 conformation within the major groove of the helix between the E-loop motif as well as in the GCAA tetraloop.[13] These metal ion interactions may be expected to stabilize the 885 conformation of H27 in the context of the ribosome.

Two experiments were performed to identify possible binding sites of metal ions within the 888 conformation of H27, a NOESY of 888_{locked} with the addition of 2 m*M* cobalt hexammine, $Co(NH_3)_6^{3+}$, which is often used as a mimic of fully hydrated magnesium ions, $Mg(H_2O)_6^{2+}$ (see Figure 7),[13,33,35,36] and a series of one dimensional (1D) spectra acquired with increasing concentrations of magnesium chloride (see Figure 8). Not unexpectedly, these experiments indicated metal ion binding within the GCAA tetraloop of the RNA, as well as in the vicinity of the G-U pairs. Strong NOEs between the G903 and U904 imino protons and $Co(NH_3)_6^{3+}$ resonance at 3.7 ppm typify specific metal ion binding in the vicinity, as has been shown previously for G-U wobble pairs in RNA.[13,33,35,36] The magnesium chloride titrations also supported the existence of metal ion binding near the G-U pairs, as well as in the GCAA tetraloop. G898(NH1), G903(NH1),

and U904(NH3) displayed relatively significant chemical shift changes with increasing magnesium ion concentration (Figures 8A and 8B) and were plotted as a function of Mg^{2+} concentration and fit with binding isotherms derived for stoichiometric, fast exchange binding between the RNA site and a Mg^{2+} ion.[37,38] The following half-titration points were extracted for G898, G903, and U904 imino protons, respectively: $Mg_{1/2}$ of 0.4 ± 0.1 m*M*, $Mg_{1/2}$ = 5.4 ± 1.2 m*M*, and $Mg_{1/2,1}$ = 2.6 ± 3.0 m*M*, and $Mg_{1/2,2}$ = 18 ± 31 m*M*.

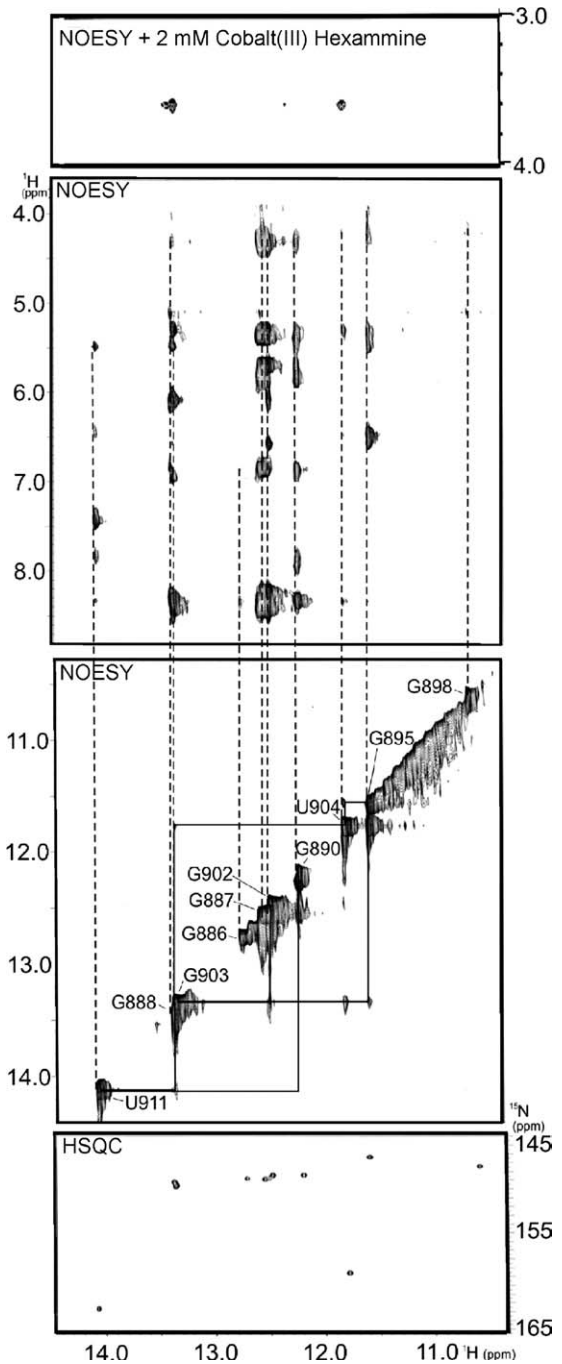

This evidence for inner-sphere Mg^{2+} binding within the tetraloop is consistent with our previous studies of the 885 conformation[13] and is well-documented in studies of other RNAs.[31–34]

The internal loop region is an asymmetric loop featuring three unpaired nucleotides opposed on the opposite strand by four unpaired nucleotides; five of the seven bases in the asymmetric internal loop are adenines. Multivalent metal ions have been shown in simulations to associate strongly with the N7 of purines,[39] and many RNA crystal structures depict $Mg(H_2O)_6^{2+}$ within the major groove, frequently hydrogen bonded through the first-shell water molecules to purine N7 groups.[40] Therefore, four ^{1}H-^{15}N HSQC experiments, optimized for observation of H8-N7 aromatic proton-nitrogen correlations, were performed at specific Mg^{2+} concentrations to investigate Mg^{2+} interactions within the internal loop of 888_{locked}. Figure 9A depicts two superimposed regions of ^{1}H-^{15}N HSQC spectra showing purine H8-N7 at 0 m*M* and 4.7 m*M* Mg^{2+}. Upon addition of the saturating concentration of 4.7 m*M* Mg^{2+}, resonances belonging to nucleotides within the helical stem regions of the molecule broaden slightly, all observable H8 resonances shift downfield by <0.1 ppm, and N7 resonances shift downfield by <1.5 ppm. A notable exception is A900(N7), the resonance of a tetraloop base, which shifts downfield by more than 2 ppm, providing further support for a Mg^{2+} binding site within the GCAA tetraloop, similar to that in the H27 885 conformation.[13] In addition, at 4.7 m*M* Mg^{2+}, the following N7H8 resonances, observed in the absence of Mg^{2+}, were lost: G886, A892, G898, A906, and A908. This observation is most probably due to broadening of these resonances, caused by nonspecific Mg^{2+} binding in the vicinity of the N7 and/or H8 purine groups.

FIGURE 7 Two-dimensional (2D) NMR spectra used to assign imino proton resonances in 888_{locked}. Imino-amino and imino-imino regions of a NOESY of 888_{locked} are shown in the center two panels, acquired with a 150-ms mixing time. Solid lines represent connectivities between nucleotides demonstrating imino-imino NOEs; dashed lines connect imino-amino NOEs with imino resonance positions on the diagonal, where imino proton resonance assignments are labeled. The imino region of a ^{1}H-^{15}N HSQC spectrum, bottom panel, unambiguously distinguishes N3 resonances of U's (downfield, 156-162 ppm) from N1 resonances of G's (upfield, 146-149 ppm). The top panel shows a portion of a 350-ms mixing time NOESY of 888 acquired with 2 m*M* cobalt hexammine, in which strong cross peaks are evident between individual imino proton resonances and the averaged cobalt hexammine signal at ~ 3.7 ppm. NMR data were processed with NMRPipe, and spectra were visualized using NMRDraw software.

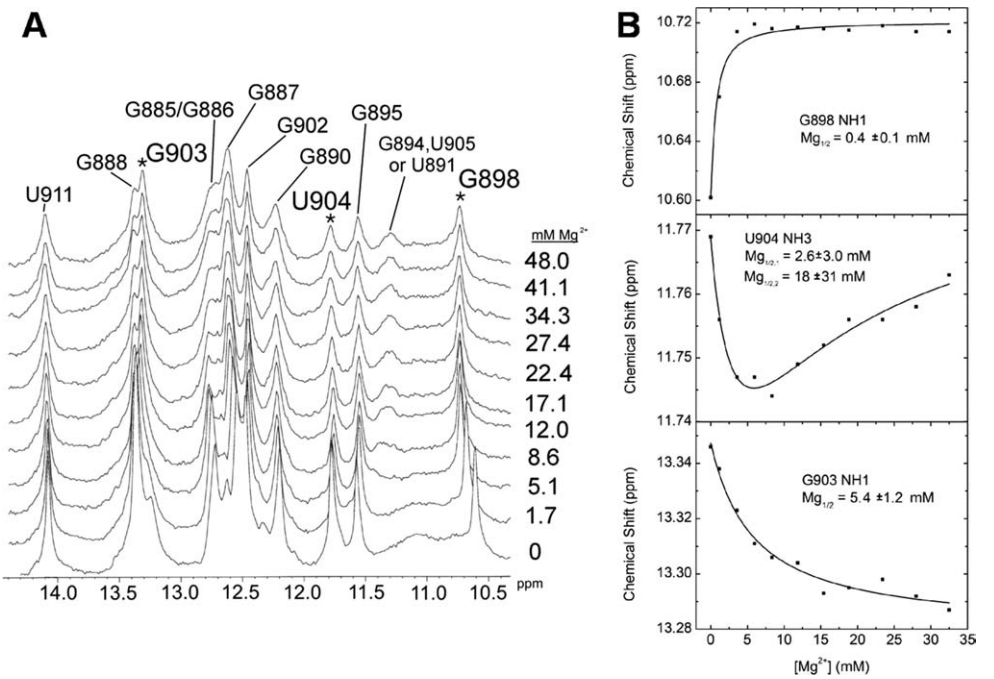

FIGURE 8 NMR-detected magnesium titrations of 888_{locked}. (A) Stacked imino proton spectra acquired with increasing Mg^{2+} concentration, as indicated. Imino proton resonance assignments are labeled; those belonging to G898, U904, and G903 are labeled with asterisks. (B) Plots of chemical shift for imino resonances in 888_{locked} as a function of Mg^{2+} concentration. Curves are shown for imino resonances belonging to G898, U904, and G903, which are well fit with binding isotherms describing a one metal per site model. Individual resonance positions were found at each metal ion concentration using the peak finder utility in NMRDraw software, and defining parameters for both a reasonable threshold for positive peak detection and a χ^2 probability threshold for noise peak rejection by χ^2 test.

Interestingly, perhaps the most informative data from the ^1H-^{15}N HSQC Mg^{2+} titration experiments arise from incidental adenine H2-N1 correlations (Figure 9A). These appear as doublets in the spectra because of splitting in the proton dimension, since decoupling was optimized for observation of H8-N7 correlations. H2-N1 resonances are not observed for all adenines within the internal loop, most likely because of severe line broadening due to dynamics in this region. However, at 0 m*M* Mg^{2+}, resonances from tetraloop adenines A900 and A901 were observed, as well as an H2-N1 correlation assigned to loop nucleotide A892. Upon addition of saturating Mg^{2+}, the A900 resonance shifts upfield by $\sim$ 1 ppm in the nitrogen dimension, and 0.1 ppm in the proton dimension, and the A901 resonance is no longer observed. The A892 resonance, by contrast, shifts downfield in the nitrogen dimension by $\sim$ 0.5 ppm and in the proton dimension by $>$0.2 ppm. Additionally, the A908 internal loop nucleotide, which does not give rise to a H2-N1 correlation in the absence of Mg^{2+}, displays a strong resonance in the presence of saturating Mg^{2+} (Figure 9A), suggesting metal ion binding in the vicinity, or that internal loop architecture and/or dynamics are altered upon addition of Mg^{2+}. The A892(H2) proton chemical shift was plotted as a function of Mg^{2+} and fit with a single metal ion per site binding isotherm (Figure 9B).[37,38] The Mg^{2+} half-titration point extrapolated from the fit is $Mg_{1/2} = 1.7 \pm 0.3$ m*M*. Shifts in nitrogen spectra may be caused by Mg^{2+} coordination, conformation changes, or dynamics, whereas carbon spectra are predominantly affected by dynamics and structure, since magnesium ions will coordinate directly with nitrogens. The aromatic region of a ^1H-^{13}C spectrum (Supporting Information Figure 1), which contains 10 m*M* $MgCl_2$ depicted general broadening of resonances, resulting in the disappearance of a few resonances and a decrease in the resolution and quality of the spectrum. In general, only minor shifting of resonances is observed in this spectrum, as compared with the ^1H-^{15}N HSQC (Figure 9A), with the exception of the A908 C2-H2 resonance that shifts by more than 0.5 ppm downfield. This suggests that the changes we observe in the ^1H-^{15}N HSQC are likely to be caused by Mg^{2+} association, with the exception of the emergence of the A908 H2-N1 resonance, which may result from reorientation of this base within the internal loop.

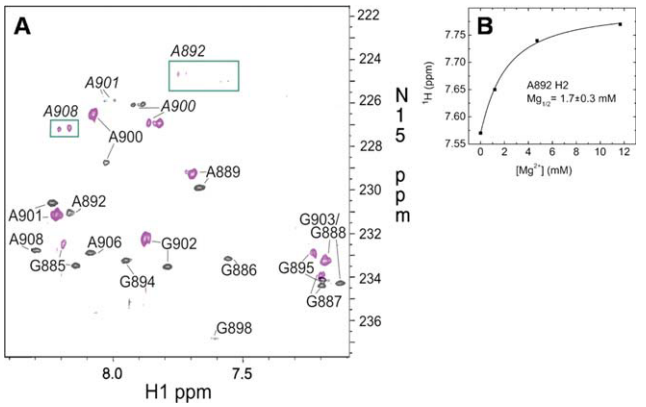

FIGURE 9 NMR evidence for Mg^{2+} binding within the internal loop of the H27 888 construct. (A) ^{1}H-^{15}N HSQC spectra displaying aromatic purine H7-N7 correlations and adenine H2-N1 correlations; spectra are superimposed; black resonances correspond to 0 m*M* Mg^{2+} solution conditions, and magenta resonances represent those acquired in the presence of 4.7 m*M* Mg^{2+}. H8-N7 resonances are labeled; adenine H2-N1 correlations are italicized, and A908 and A892 H2-N1 resonances are boxed for clarity. (B) Plot of chemical shift for H27 888 construct A892 H2 proton resonance as a function of Mg^{2+} concentration. Curve shown is fit with a binding isotherm describing a one metal per site model. Individual resonance positions were found at each metal ion concentration using the peak finder utility in NMRDraw software, and defining parameters for both a reasonable threshold for positive peak detection and a χ^2 probability threshold for noise peak rejection by χ^2 test.

DISCUSSION

Overview of the 888 Conformation

Here, we report the solution NMR structure of a conformationally locked RNA representing an alternate base-pairing scheme for helix (H)27 from *Escherichia coli* 16S rRNA, in which C912 Watson–Crick base pairs with G888 instead of G885 as observed in the available ribosomal crystal structures. Traditional NOE-based methods were employed for structure determination, and an ensemble of 50 lowest-energy structures were refined with RNA database potentials and RDCs.[23,25] These lowest energy structures consist of a A-form "lower" stem and a predominantly A-form "upper" stem capped with a GCAA tetraloop. RDC refinement of the low-energy structures revealed a nearly straight linear helix, with very little bend between the upper and lower stems. Bridging the two stems is an asymmetric internal loop, which displayed conformational variability because of a smaller number of conformational restraints in this region relative to the stem regions. We attribute the lower number of NOE restraints in the internal loop region to a higher degree of dynamics throughout the internal loop. TOCSY H1′-H2′ cross peaks indicated ring flexibility, specifically, C2′-endo/C3′-endo equilibrium among many of the internal loop riboses (See Supporting Information). In addition, ^{1}H-^{15}N NOE measurements (see Supporting Information) are consistent with increased motion in the vicinity of G904 and G895, which are bases adjacent to the loop.

The 888 conformation of H27 RNA expectedly binds Mg^{2+} ions, and the absence of large changes in resonance positions and/or NOE patterns indicates that metal ion binding does not significantly change the overall structure of 888_{locked}. Three locations were identified as involved in metal binding: the GCAA tetraloop, the tandem G-U wobble pair, and the A892/A908 region.

Comparison of the 888 and 885 Conformations

Helix 27 is a highly conserved, albeit relatively small helix adjacent to the decoding center of the small ribosomal subunit. Our 888_{locked} solution structure, which favors the 888 conformation by introducing cytosines at positions 913, 914, has many similarities to its conformational counterpart but in some ways is strikingly different from the 885 conformation observed in crystal structures of the complete 30S ribosomal subunit. The perhaps most obvious structural difference is the global length of the helix. With the three-nucleotide shift from a C912-G885 pair to a C912-G888 pair, and subsequent shifting of lower stem base pairs and internal loop conformation, an overall lengthening of the helix occurs. Figure 10

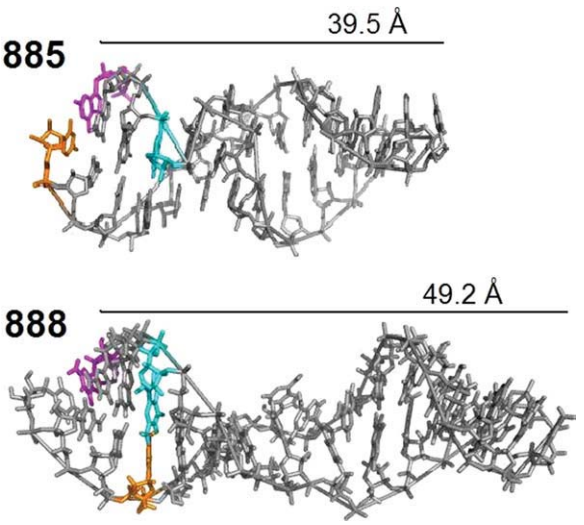

FIGURE 10 Two conformations for Helix 27. The top structure represents nucleotides G885-C912 taken from the crystal structure of the 30S ribosomal subunit of *Thermus thermophilus* (PDB ID 1FJG, numbering scheme is from *Escherichia coli*). The bottom structure is a representative NMR structure from the lowest energy 888_{locked} structure ensemble. G886-C899 interphosphorous distances are shown for each structure. This figure was created using PyMol software.

compares a representative low energy structure of 888_{locked} with the H27 885 conformation from the crystal structure of the 30S ribosomal subunit of *Thermus thermophilus* (PDB ID 1FJG[29]). In both structures, G885 is colored magenta, G888 is colored cyan, and C912 is colored orange. Measurements were taken in each helix from the phosphorus atom of G886 at the base of the helix to that of C889 at the apex of the tetraloop (using the numbering scheme from *E. coli*). The G886-C889 interphosphorus distance of the 888 conformation is 49.2 Å, compared with 39.5 Å for the 885 conformation, an increase of nearly 25%. It should be noted that this observed $\sim$ 10 Å difference in length between the two conformers may be due in part to the low NOE density for the internal loop region. Additionally, Mg^{2+} interacts with the internal loop, which may affect the overall length of the internal loop; the structure presented here was determined from data collected in the absence of Mg^{2+}. It is also difficult to compare the length of the 885 conformation within the context of the crystallized ribosome with the 888 conformation in solution, as the energy minimization protocol used to arrive at the final NMR ensemble structure can sometimes extend the structure. These limitations may artificially extend this region of the structure somewhat so that the $\sim$ 10 Å difference should be viewed as an upper limit. Nevertheless, the final 888_{locked} calculated structures were cross-validated with 30% of the RDCs measured and had R_{free} values <30, indicating that the global calculated structural parameters agree well with the solution structure and justifying a comparison of the lengths of the two available structures of the H27, the 885 conformation, as it exists in the context of a crystallized ribosome, and the 888 conformation, as it exists isolated in solution.

The second most significant structural difference between the two H27 conformations is the nucleotide arrangement within the internal loop. The upper stem structures in both the 885 and 888 conformers are essentially identical, consisting of a GCAA tetraloop closed by two C-G Watson–Crick pairs, flanked by tandem G-U wobble pairs. The lower stems of both molecules are very similar as well; although the number and type of base pairs vary (for example, the 888 lower stem is longer than the 885 lower stem, and the 885 lower stem contains one G-U wobble pair), they both adopt a stable and predominantly A-form helix in which a stretch of purines on one strand pairs with a stretch of pyrimidines on the opposing strand. The nucleotides of the internal loop region of the 885 conformation do not adopt an asymmetric internal loop conformation, as seen in the 888 conformation; instead they form a well-characterized series of non-Watson–Crick pairs and hydrogen bonds called a loop E motif.[41] This loop E motif is very A-rich. When H27 is locked in the 888 conformation, the stable loop E motif cannot form, since several of the 885 loop E nucleotides on the strand opposing A909-A907 become part of the 888 lower helical stem, involved in Watson–Crick base pairs.

Why Is the 888 Conformation of H27 not Observed in the Context of the Intact 30S Ribosomal Subunit?

Mutational studies once predicted that reorganization of the base pairing scheme of this helix, in which C912 alternately pairs in Watson–Crick fashion with G885 and G888, was necessary for proper decoding of the message.[3] However, many crystal structures emerged depicting various "hyperaccurate" and "error-prone" 30S ribosomal subunit phenotypes, and ribosomes in both "open" and "closed" conformations, and all showed helix 27 adopting the same 885 conformation.[5,6] In 2004, subsequent follow-up studies by the Dahlberg group revealed that synergistic effects with selectable markers were responsible for the original observations, and conformational change within helix 27 was not necessary for maintenance of translation fidelity,[7] corroborating the crystal structures.

Previous NMR and FRET studies by our group supported the existence of two conformations for an isolated *E.coli* H27 sequence in solution, with nearly equal populations, and a dynamic equilibrium between the two structures with an interconversion rate on the millisecond timescale.[4] Why is the 888 conformation, which the H27 sequence so readily adopts in solution, absent in the context of intact 30S ribosomal subunits? Helix 27 makes very few protein contacts as compared with other small ribosomal subunit RNA helices; its only near-contact is with the relatively unstructured cationic N-terminal tail of S12 that extends into a pocket adjacent to H27 (Figure 1A, shown in cyan), where lysine 21 lies within 3.7 Å of each one nonbridging phosphate oxygen of A908 and A909.[29,42] This long-range electrostatic interaction may stabilize the 885 over the 888 conformation in the context of the ribosome, even though the base pairing patterns are close to isoenergetic in the isolated helix.[4] The solution structure of the 888 conformation, when compared with the structure of the 885 conformation from crystal structures, provides some additional insight into possible reasons for the relative stability of the 885 over the 888 conformation in the context of the ribosome.

Within the 30S subunit, the highly conserved GCAA tetraloop of H27 docks into the minor groove of the helix (H)24 769-810 region (Figure 1A, shown in bright and dark green, on right of panel).[42–44] Mutations that interfere with the H27-H24 interaction have been shown to impair translational accuracy, interfere with subunit association since they

disrupt the intersubunit bridge B2a formed between H27 and 23S rRNA H67, and decrease overall ribosome activity.[45] Additionally, compensatory mutations in another helix, H1, can negate the deleterious effects of an A900G mutation in H27, implying a functional relationship between these regions, although they show no close contact in crystal structures.[46] At the opposite end of H27, at the 3′ terminus, nucleotides 913-920 interact with the loop region of H1. This interaction forms helix 2, the core of the central pseudoknot of the 30S subunit. Destabilization of the central pseudoknot results in faulty subunit association.[47,48] Therefore, interhelix interactions at both the terminus and the tetraloop regions of H27 must be maintained for proper ribosome function. As discussed earlier, the 888 conformation is likely to be somewhat longer than the 885 conformation (up to ∼ 25% by our measurements of the available structures), and it is thus plausible that such an extended H27 would not be accommodated in a biologically active ribosome.

In summary, we have solved by NMR the solution structure of an alternate base-pairing conformation of helix 27 from 16S rRNA from *E. coli*. This conformation was once thought to be of functional significance, since switching between this base pairing scheme, in which C912 pairs with G888, and its analogue, in which C912 instead pairs with G885, was proposed to be necessary for proper decoding of mRNA during bacterial translation. Our lowest energy structures depict a conformationally locked 888 conformation that is up to 25% longer than the 885 conformation observed in crystal structures, which offers a plausible explanation for why this conformation, which the isolated H27 sequence readily adopts in solution, is absent in the context of the sterically constraining 30S subunit.

MATERIALS AND METHODS

Preparation of NMR Samples

The 31-nucleotide 888_{locked} NMR construct representing the 888 conformer of H27 (5′-GGG GAG UAC GGC CGC AAG GUU AAA ACU CCC C-3′) (Figure 1B) was designed with the addition of three non-native C nucleotides at the 3′ helix terminus of the helix 27 sequence from *Escherichia coli* 16S ribosomal RNA to stabilize the 888 conformation and prevent it from conformational switching. The construct was transcribed in vitro from a fully double-stranded DNA template with a T7 RNA polymerase promoter region, as described previously.[4] Isotopically enriched nucleotide triphosphates (NTPs) (Silantes) were substituted for unlabeled NTPs for transcription of a uniformly $^{13}C/^{15}N$-labeled 888 molecule. After incubation at 37°C overnight, EDTA was added to all transcription reactions to a final concentration exceeding 60 m*M*, and the resulting mixture was extracted with an equal volume of phenol and two subsequent extractions with a 24:1 $CHCl_3$:isoamyl alcohol mixture. The protein-free extracts were then concentrated in Centricon-3 filter devices (Amicon), and the desired transcription product was purified by gel electrophoresis on a denaturing, 8*M* urea, 20% polyacrylamide gel. The gels were UV-shadowed, and bands corresponding to the 31-nt H27 888 construct were excised, crushed, and the RNA eluted by soaking in a sterile-filtered 5 m*M* EDTA solution. The NMR constructs were further purified by anion exchange chromatography using DEAE Sephadex resin (Sigma), exchanged into NMR buffer (10 m*M* NaP_i, pH 6.4, 0.1 m*M* EDTA, 50 m*M* NaCl), and concentrated to ∼ 200 μL. NMR buffer was added to a final volume of 225–250 μL, including the addition of 99.9% ^2H_2O (Aldrich or Cambridge Isotope Labs) to an amount equaling 5% (v/v) of the total sample volume. The NMR sample of the unlabeled 888 construct was dried down after completion of preliminary experiments and resuspended in "100%" ^2H_2O (Cambridge Isotope Labs) for observation of nonexchangeable protons only. Final RNA concentrations for the samples ranged from 0.8 to 1.6 m*M*, as quantified by UV absorption, and ^2H_2O-matched microvolume NMR tubes (Shigemi) were used during collection of all NMR spectra.

NMR Spectroscopy

Proton and heteronuclear experiments were performed using an 800 MHz Varian Inova spectrometer equipped with a triple resonance ^1H, ^{13}C, ^{15}N probe with *Z*-gradients or a Bruker Avance 600 MHz spectrometer equipped with a triple-resonance 5-mm cryogenic probe. Homonuclear spectra of exchangeable protons were collected at 277 K; all other data were obtained at either 293 or 303 K (reported chemical shifts were obtained at 293 K; see Supporting Information). Proton spectra and magnesium chloride titrations were recorded as described in earlier studies,[13] and all heteronuclear experiments, including ^{15}N spin-lattice and spin-spin relaxation and $\{^1H$-^{15}N NOE$\}$ measurements, were performed as previously described,[49] except where noted. RDCs were obtained through measurement of $^1J_{CH}$ for the following atom pairs: C2-H2, C5-H5, C6-H6, C8-H8, and C1′-H1′. Splittings were measured in the indirect dimension of spectra acquired using a constant-time spin-state-selective coherence-transfer transverse relaxation optimized spectroscopy (TROSY) experiment,[50] in both the presence and absence of ∼ 19.4 mg/mL Pf1 phage (see Supporting Information for RDC tables). Approximate filamentous phage concentration in the sample was determined experimentally by measurement of the splitting in the $^1HO^2H$ signal in a 1D ^2H spectrum.[51] All data were processed using NMRPipe and NMRDraw,[52] and spectra were visualized and assigned using SPARKY 3.[53] Relaxation data were additionally analyzed using NMRView.[54] 1D proton spectra acquired throughout the magnesium chloride titrations were processed with NMRPipe using a solvent filter and a cosine-bell apodization function, and zero-filled once before Fourier transforming; NMRDraw was used to visualize each spectrum and detect peaks.[52] Data were then reprocessed using Bruker software to create the stacked plots shown in Figure 8. Plots of chemical shift versus Mg^{2+} concentration were fit with the following binding isotherm for a system in fast exchange, where the RNA concentration is of the same magnitude as the metal ion concentration:

$$\delta_{obs} = \delta_f + \left((\delta_b - \delta_f) \frac{\left\{ \left[[ion]_t + [RNA]_t + Mg_{1/2} \right] - \sqrt{\left([ion]_t + [RNA]_t + Mg_{1/2} \right)^2 - \left(4\,[RNA]_t\,[ion]_t \right)} \right\}}{2\,[RNA]_t} \right)$$

δ_{obs} is the observed chemical shift, δ_f is the chemical shift of the unbound imino proton, δ_b is the chemical shift of the fully bound proton, $[ion]_t$ is the total magnesium ion concentration, $[RNA]_t$ is the RNA concentration, and $Mg_{1/2}$ is the apparent magnesium ion dissociation constant. The biphasic curve of the U904(NH3) resonance position versus molar equivalents of magnesium chloride was fit with the following composite equation:

$$\delta_{obs} = \left\{ \delta_{f1} + \left((\delta_{b1} - \delta_{f1}) \frac{\left\{ \left[[ion]_t + [RNA]_t + Mg_{1/2,1} \right] - \sqrt{\left([ion]_t + [RNA]_t + Mg_{1/2,1} \right)^2 - \left(4\,[RNA]_t\,[ion]_t \right)} \right\}}{2\,[RNA]_t} \right) \right\}$$

$$- \left\{ \delta_{f2} + \left((\delta_{b2} - \delta_{f2}) \frac{\left\{ \left[[ion]_t + [RNA]_t + Mg_{1/2,2} \right] - \sqrt{\left([ion]_t + [RNA]_t + Mg_{1/2,2} \right)^2 - \left(4\,[RNA]_t\,[ion]_t \right)} \right\}}{2\,[RNA]_t} \right) \right\}$$

so that two apparent dissociation constants, $Mg_{1/2,1}$ and $Mg_{1/2,2}$, were extracted; these were similar to those calculated from two curves fit independently to the low and high Mg^{2+} concentration data points, respectively. Chemical shifts reported are accurate within the digital resolution of the spectrum, or sweep width (ppm) divided by the number of acquisition points. The digital resolution in the Mg^{2+} titration data is therefore 0.004 ppm.

Structural Restraints and Calculations

Energies for 298 random starting structures generated from the 888_{locked} sequence information were minimized in X-PLOR using a torsion-angle molecular dynamics (MD) (TAMD) protocol,[21,55,56] followed by a conjugate gradient minimization stage. The TAMD protocol used a purely repulsive van der Waal's function and a soft square-well NOE restraint function.[57] Distance restraints, with the exception of imposed Watson–Crick hydrogen bonds, were obtained by evaluation of NOESY cross peak intensities at 50, 200, 350, 450, and 600 ms mixing times at either 293 or 303 K and assigned to the following intensity ranges: strong, 1.5–3.0 Å; medium, 2.0–4.2 Å; weak, 2.5–5.4 Å; and very weak, 3.0–6.5 Å. Intensities were calibrated against pyrimidine H5-H6 NOESY cross peak intensities representing a known distance of ~ 2.45 Å. Hydrogen bond distance restraints were also imposed between donor and acceptor atoms within the GNRA tetraloop, as documented by Jucker et al.[16] Backbone dihedral angles α, β, γ, ε, and ζ were restrained to model A-form values for upper and lower stem nucleotides G885-A889, G895-C896, G903-U904, and U911-C915. Dihedral angles α, β, and γ of G890, C897, and U905 and also ε and ζ of G894, G902, and C910 were additionally restrained in this manner. The glycosidic χ dihedral angle for each nucleotide in the sequence was restrained to reflect the *anti*-conformation, since no strong intranucleotide H6/H8-H1′ NOEs signifying the presence of any *syn* base conformations were observed at the 50-ms mixing time. The nucleotide riboses displaying strong H1′-H2′ cross peaks in TOCSY spectra, indicating $J_{H1'\text{-}H2'} > 7$ Hz, were restrained to the C2′-endo conformation; all others were restrained to C3′-endo parameters (see Supporting Information).

The 50 lowest energy structures were then refined with XPLOR-NIH[22] as described by Clore and coworkers, using RNA database potentials and RDCs.[23,25] Of the 48 RDCs measured, only those $^1D_{CH}$ values obtained from nucleotides within the structurally well-defined helical stem regions of the molecule were used in refinement. Of those, 20 (or ~ 70%) were applied as restraints, and the remaining 6 (or ~ 30%) were used for cross-validation (see Supporting Information).[25] Structures were refined using two independent techniques, one using axial and rhombic alignment tensors D_a and R defined separately for the upper stem and the lower stem of the molecule and one using a single set of globally defined alignment tensors. Structures were nearly identical, although R_{free} values were slightly lower for the set of structures that used two sets of

alignment tensors, one for the upper and one for the lower helical stem of the molecule. These 13 structures with R_{free} values <30 comprise the final ensemble structure reported here.

The authors thank Dr. Hashim Al-Hashimi, Dr. Qi Zhang, and Dr. Ananya Majumdar for invaluable assistance with NMR data collection, Dr. Alex Hansen for instruction with ^{15}N-^{1}H NOE analyses, Dr. Anthony Manzo and Dr. Todd Raeker for computer support, Dr. Alex Kurochkin for NMR spectrometer maintenance, and all current and former members of the Walter group for helpful discussions. The authors also thank anonymous reviewers for their insightful comments. The H27 888_{locked} ensemble structures have been submitted to the Protein Data Base.

REFERENCES

1. Cannone, J. J.; Subramanian, S.; Schnare, M. N.; Collett, J. R.; D'Souza, L. M.; Du, Y.; Feng, B.; Lin, N.; Madabusi, L. V.; Muller, K. M.; Pande, N.; Shang, Z.; Yu, N.; Gutell, R. R. BMC Bioinformatics 2002, 3, 2.
2. Woese, C. R.; Gutell, R.; Gupta, R.; Noller, H. F. Microbiol Rev 1983, 47, 621–669.
3. Lodmell, J. S.; Dahlberg, A. E. Science 1997, 277, 1262–1267.
4. Hoerter, J. A.; Lambert, M. N.; Pereira, M. J.; Walter, N. G. Biochemistry 2004, 43, 14624–14636.
5. Vila-Sanjurjo, A.; Ridgeway, W. K.; Seymaner, V.; Zhang, W.; Santoso, S.; Yu, K.; Cate, J. H. Proc Natl Acad Sci U S A 2003, 100, 8682–8687.
6. Ogle, J. M.; Murphy, F. V.; Tarry, M. J.; Ramakrishnan, V. Cell 2002, 111, 721–732.
7. Rodriguez-Correa, D.; Dahlberg, A. E. RNA 2004, 10, 28–33.
8. Andersen, A. A.; Collins, R. A. Mol Cell 2000, 5, 469–478.
9. Andersen, A. A.; Collins, R. A. Proc Natl Acad Sci U S A 2002, 98, 7730–7735.
10. Staple, D. W.; Butcher, S. E. Nucleic Acids Res 2003, 31, 4326–4331.
11. Staple, D. W.; Butcher, S. E. J Mol Biol 2005, 349, 1011–1023.
12. Caetano-Anolles, G. Nucleic Acids Res 2002, 30, 2575–2587.
13. Lambert, M. N.; Hoerter, J. A.; Pereira, M. J.; Walter, N. G. RNA 2005, 11, 1688–1700.
14. Wijmenga, S.; Mooren, M. H. C. In NMR of Macromolecules: A Practical Approach; Roberts, G. C. K., Ed.; Oxford University Press: Oxford, 1993; pp 217–288.
15. Chang, L. H.; Marshall, A. G. Biochemistry 1986, 25, 3056–3063.
16. Jucker, F. M.; Heus, H. A.; Yip, P. F.; Moors, E. H.; Pardi, A. J Mol Biol 1996, 264, 968–980.
17. Patel, D. J.; Hilbers, C. W. Biochemistry 1975, 14, 2651–2656.
18. Lukavsky, P. J.; Kim, I.; Otto, G. A.; Puglisi, J. D. Nat Struct Biol 2003, 10, 1033–1038.
19. Flinders, J.; Dieckmann, T. J Mol Biol 2004, 341, 935–949.
20. Majumdar, A.; Kettani, A.; Skripkin, E.; Patel, D. J. J Biomol NMR 2001, 19, 103–113.
21. Brunger, A. T. X-PLOR Version 3.851. A System for X-ray Crystallography and NMR; Yale University Press: New Haven, CT, 1996.
22. Schwieters, C. D.; Kuszewski, J. J.; Tjandra, N.; Clore, G. M. J Magn Reson 2003, 160, 65–73.
23. Kuszewski, J.; Gronenborn, A. M.; Clore, G. M. Protein Sci 1996, 5, 1067–1080.
24. Clore, G. M.; Gronenborn, A. M.; Tjandra, N. J Magn Reson 1998, 131, 159–162.
25. Clore, G. M.; Kuszewski, J. J Am Chem Soc 2003, 125, 1518–1525.
26. Tolbert, B. S.; Miyazaki, Y.; Barton, S.; Kinde, B.; Starck, P.; Singh, R.; Bax, A.; Case, D. A.; Summers, M. F. J. Biomol. NMR 2010, 47, 205–219.
27. Saenger, W. In Principles of Nucleic Acid Structure; Cantor, C., Ed.; Springer-Verlag: New York, 1983, p 244.
28. Brodersen, D. E.; Clemons, W. M., Jr.; Carter, A. P.; Morgan-Warren, R. J.; Wimberly, B. T.; Ramakrishnan, V. Cell 2000, 103, 1143–1154.
29. Carter, A. P.; Clemons, W. M.; Brodersen, D. E.; Morgan-Warren, R. J.; Wimberly, B. T.; Ramakrishnan, V. Nature 2000, 407, 340–348.
30. Ogle, J. M.; Brodersen, D. E.; Clemons, W. M., Jr.; Tarry, M. J.; Carter, A. P.; Ramakrishnan, V. Science 2001, 292, 897–902.
31. Hermann, T.; Westhof, E. Structure 1998, 6, 1303–1314.
32. Maderia, M.; Horton, T. E.; DeRose, V. J. Biochemistry 2000, 39, 8193–8200.
33. Rudisser, S.; Tinoco, I., Jr. J Mol Biol 2000, 295, 1211–1223.
34. Mundoma, C.; Greenbaum, N. L. J Am Chem Soc 2002, 124, 3525–3532.
35. Kieft, J. S.; Tinoco, I., Jr. Structure 1997, 5, 713–721.
36. Gdaniec, Z.; Sierzputowska-Gracz, H.; Theil, E. C. Biochemistry 1998, 37, 1505–1512.
37. Lian, L.-Y.; Roberts, G. C. K. In NMR of Macromolecules: A Practical Approach; Roberts, G. C. K., Ed.; Oxford University Press: Oxford, 1993; pp 153–181.
38. Gonzalez, R. L., Jr.; Tinoco, I., Jr. J Mol Biol 1999, 289, 1267–1282.
39. Rulisek, L. S. J. J Phys Chem 2003, 107, 1913–1923.
40. Draper, D. E.; Grilley, D.; Soto, A. M. Annu Rev Biophys Biomol Struct 2005, 34, 221–243.
41. Leontis, N. B.; Westhof, E. J Mol Biol 1998, 283, 571–583.
42. Schuwirth, B. S.; Borovinskaya, M. A.; Hau, C. W.; Zhang, W.; Vila-Sanjurjo, A.; Holton, J. M.; Cate, J. H. Science 2005, 310, 827–834.
43. Schluenzen, F.; Tocilj, A.; Zarivach, R.; Harms, J.; Gluehmann, M.; Janell, D.; Bashan, A.; Bartels, H.; Agmon, I.; Franceschi, F.; Yonath, A. Cell 2000, 102, 615–623.
44. Wimberly, B. T.; Brodersen, D. E.; Clemons, W. M., Jr.; Morgan-Warren, R. J.; Carter, A. P.; Vonrhein, C.; Hartsch, T.; Ramakrishnan, V. Nature 2000, 407, 327–339.
45. Belanger, F.; Gagnon, M. G.; Steinberg, S. V.; Cunningham, P. R.; Brakier-Gingras, L. J Mol Biol 2004, 338, 683–693.
46. Belanger, F.; Theberge-Julien, G.; Cunningham, P. R.; Brakier-Gingras, L. RNA 2005, 11, 906–913.
47. Brink, M. F.; Verbeet, M. P.; de Boer, H. A. EMBO J 1993, 12, 3987–3996.
48. Poot, R. A.; Pleij, C. W.; van Duin, J. Nucleic Acids Res 1996, 24, 3670–3676.
49. Zhang, Q.; Sun, X.; Watt, E. D.; Al-Hashimi, H. M. Science 2006, 311, 653–656.
50. Meissner, A.; Sorensen, O. W. J Magn Reson 1999, 139, 439–442.
51. Hansen, M. R.; Mueller, L.; Pardi, A. Nat Struct Biol 1998, 5, 1065–1074.

52. Delaglio, F.; Grzesiek, S.; Vuister, G. W.; Zhu, G.; Pfeifer, J.; Bax, A. J Biomol NMR 1995, 6, 277–293.
53. Goddard, T. D. A.; Kneller, D. G. SPARKY 3; University of California: San Francisco.
54. Johnson, B. A.; Blevins, R. A. J Biomol NMR 1994, 4, 603–614.
55. Rice, L. M.; Brunger, A. T. Proteins 1994, 19, 277–290.
56. Stein, E. G.; Rice, L. M.; Brunger, A. T. J Magn Reson 1997, 124, 154–164.
57. Newby, M. I.; Greenbaum, N. L. Nat Struct Biol 2002, 9, 958–965.
58. DeLano, W. L. The PyMOL Molecular Graphics System; DeLano Scientific LLC: San Carlos, CA, 2002.

Reviewing Editor: Sarah A. Woodson